

Modeling, Analysis, and Reduction of Radiated EMI Due to the Voltage Across Input and Output Cables in an Automotive Non-Isolated Power Converter

Juntao Yao [✉], Member, IEEE, Shuo Wang [✉], Fellow, IEEE, and Zheng Luo [✉]

Abstract—This article investigates the radiated electromagnetic interference (EMI) due to the voltage between input and output cables in a non-isolated power converter. The radiated EMI model of a non-isolated power converter is first developed and quantified based on the circuit topologies, printed circuit board (PCB) parasitics, switching waveforms, and transfer functions. Second, an antenna model is developed for converter cables based on the antenna impedance and the antenna transfer function. Third, a complete radiated EMI model is developed based on the converter’s EMI model and the cable’s antenna model. Fourth, the radiated EMI is analyzed based on the developed model. Finally, two radiated EMI noise reduction techniques, optimizing PCB layout and adding a cross capacitor, are proposed. The developed radiated EMI model and the proposed radiated EMI reduction techniques are verified with both simulations and experiments. The techniques are also extended to other two non-isolated power converter topologies when the radiated EMI is caused by the voltage between the input and output cables.

Index Terms—Electromagnetic interference (EMI), noise reduction, non-isolated power converter, PCB layout, radiated EMI.

I. INTRODUCTION

IN MODERN power electronics, with the help of high-speed semiconductor devices, switching frequencies were increased to reduce passive component size and increase power densities. However, high switching frequencies lead to high radiated electromagnetic interference (EMI) [1]–[6]. In popular non-isolated power converters, radiated EMI is an important challenge to engineers [1], [7]. Therefore, it is necessary to develop radiated EMI modeling and reduction techniques for non-isolated power converters.

The existing papers focused on the equivalent driven mechanism of the cable antenna [8], [9] and the calculation of near field emission from cables [10]. They did not investigate the

detail inside power converters, so the existing techniques did not reveal the mechanisms based on power electronics circuits, printed circuit board (PCB) layout, and switching waveforms. They cannot be directly used to help power electronics engineers for layout optimization and radiated EMI reduction. More understanding and detail analysis on the radiated EMI models for power converters in terms of converter operation principle, PCB layout, and switching waveforms will be presented in this article. For the power electronics systems with long attached power cables, the power converter behaves like a noise source and the attached power cables behave like an antenna [8]. The switching of power semiconductor devices generates excitation voltages on cables. The excitation voltage drives the cable antenna and leads to the common mode (CM) currents for EMI radiation. The radiated EMI due to CM currents on the power cables [7], [11]–[14] was predicted in the existing literature based on the superposition of the electric field generated by the distributed Hertzian dipole current segments [7]. However, the mechanisms of radiated EMI generation in the power converters were not disclosed and the techniques to reduce the radiated EMI were not developed for the converter design.

The CM noise source behavioral models were reconstructed based on external parameters such as the CM currents and CM impedances in [15] and [16]. However, those behavioral models are black-box models which have limited physical meanings, so they cannot reveal important noise generation and reduction mechanisms in power converters.

For radiated EMI analyses in power electronics, it is essentially important to develop radiated EMI models with clear physical meanings. Chen *et al.* [17] disclosed a radiated EMI mechanism: the CM noise current is coupled to the earth ground from the power converter’s voltage pulsating nodes via parasitic capacitance; the CM noise current further flows back to the power converter via the input cable, causing monopole style radiated EMI. However, the detailed relationship of the power converter’s switching operation, parasitic parameters, and the radiated EMI is not disclosed. Furthermore, if the converter topology and the test setup are complicated, the extraction of the equivalent noise source is not simple or straightforward [18]. In summary, it is assumed that the parasitic capacitance between the pulsating node and the earth ground plays a big role in driving the monopole antenna of the input cable. This assumption applies to some applications, but does not apply to other applications. For example, for the converters with both input and output cables,

Manuscript received January 4, 2021; revised May 9, 2021, July 18, 2021, and September 12, 2021; accepted November 5, 2021. Date of publication November 17, 2021; date of current version January 19, 2022. This work was supported by the Monolithic Power Systems, Inc. Recommended for publication by Associate Editor F. Costa. (*Corresponding author: Shuo Wang.*)

Juntao Yao and Shuo Wang are with the Department of Electrical and Computer Engineering, University of Florida, Gainesville, FL 32611-7011 USA (e-mail: juntaoyao@outlook.com; shuowang@ieee.org).

Zheng Luo is with Monolithic Power Systems Inc., San Jose, CA 95119 USA (e-mail: zheng.luo@monolithicpower.com).

Color versions of one or more figures in this article are available at <https://doi.org/10.1109/TPEL.2021.3128628>.

Digital Object Identifier 10.1109/TPEL.2021.3128628

the antenna will be modeled as a dipole antenna. The CM current on the dipole antenna is generated due to the voltage between input and output cables instead of due to the pulsating voltage via the parasitic capacitance to the ground [9]. In [19], the radiated EMI is predicted based on the measured excitation voltage and the analysis of the cable antenna. However, in [19], the effects of power converter PCB layout and its parasitics on the radiated EMI are not quantified, and there is no guideline on how to improve the power converter design so as to reduce the radiated EMI.

For isolated power converters, the radiated EMI models are developed with clear physical meanings based on the power converter EMI model and the cable antenna model in [18] and [20]. It is revealed that the antenna is driven by the voltage difference between the primary ground and the secondary ground, which is caused by the unbalanced transformer parasitics [20]–[23] and impacted by the capacitive couplings between pulsating nodes and power cables [20]. Based on the developed models, noise reduction techniques are developed. These techniques include a transformer coaxial shielding winding technique, a high-frequency lossy CM choke design technique, and an improved converter shielding technique [20], [21], [24] for radiated EMI reduction. However, in non-isolated power converters, dedicated research has not been fully conducted to develop radiated EMI models with clear physical meanings and radiated EMI reduction techniques.

The methodology employed here for the radiated EMI analysis particularly with the parasitics is significantly different from that used in conducted EMI analysis. For conducted EMI, the CM EMI noise propagates through parasitic capacitances from switching devices, to heat-sinks, and to the earth ground. After that, the CM conducted EMI noise flows to line impedance stabilization networks (LISNs), which allows the noise to be directly measured [25]–[27], and finally back to the power converters. On the other hand, the radiated EMI is represented with the electric field emitted from power converters. The driving voltage of the radiation is the voltage drop of high frequency switching currents on critical parasitic impedance across the input and output cables. For automotive applications, standard CISPR 25 is followed for the measurements in this article.

The contributions of this article include the following.

- 1) We developed and quantified a radiated EMI model with clear physical meanings for a non-isolated power converter, which can predict the radiated EMI and reveal the impact of the parasitics of PCB layout on the radiated EMI; the model can help power electronics engineers to predict the radiated EMI in the converter design stage.
- 2) Based on the developed model, we developed two techniques for radiated EMI reduction, including PCB layout optimization and cross capacitor implementation.
- 3) The developed techniques are extended to other two non-isolated converter topologies.

The rest of this article is organized as follows. In Section II, a radiated EMI model is developed, quantified, and verified. For the procedure of the radiated EMI modeling and prediction for non-isolated power converters, the noise model of the power converter is first developed in Section II-A, the cable antenna

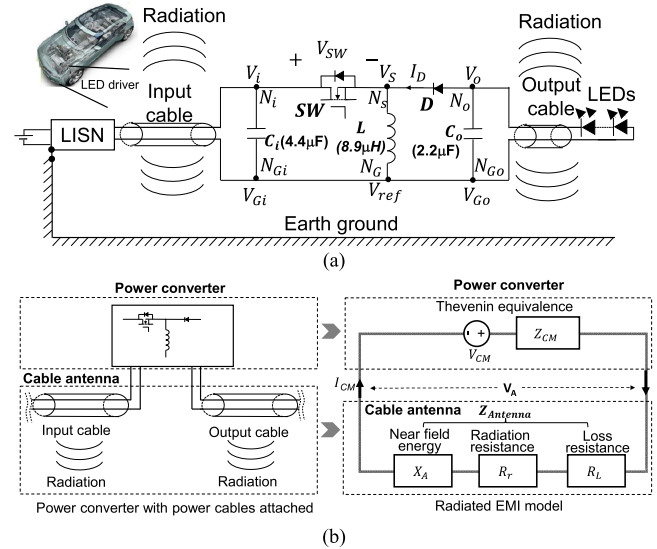


Fig. 1. Radiated EMI model of a power converter. (a) Non-isolated power converter used as an automotive LED driver. (b) General radiated EMI model for a power converter [6], [15], [17], [19].

model is then developed in Section II-B, and in Section II-C, the developed models are integrated into the radiated EMI model for radiated EMI prediction and analysis. In Section III, radiated EMI reduction techniques are proposed and experimentally verified. In Section IV, the developed technique is extended to other two non-isolated power converter topologies when the dominant radiated EMI is due to the voltage between the input and output cables. Finally, Section V concludes this article.

II. TECHNIQUE OF MODELING AND ANALYSIS OF RADIATED EMI IN A NON-ISOLATED POWER CONVERTER

Fig. 1(a) shows an EMI measurement setup for a buck-boost converter employed as an automotive LED driver. The main switch and controller is MP2483 from Monolithic Power Systems. The diode is B360A from Diodes Inc. The voltage source is a 12-V battery. The switching frequency is 700 kHz. The load is four LEDs in series with 2.85 V forward voltage of each, and the load current is 500 mA. The converter has a 1.5 m input power cable and a 0.5 m output power cable. The cables are composed of two twisted AWG16 wires. As analyzed in [19], the input and output cables behave like an antenna to radiate EMI. The input cable is connected to nodes N_i and N_{Gi} and the output cable is connected to nodes N_o and N_{Go} on the PCB. The voltage of node N_G is taken as a reference.

The general radiated EMI model has been developed in [6], [15], [17], and [19], as shown in Fig. 1(b). The converter can be modeled as an equivalent CM noise voltage source V_{CM} in series with an equivalent source impedance Z_{CM}. Here, the CM noise voltage source is defined as the equivalent Thevenin's noise voltage source which directly generates CM current flowing through input and output cables leading to the radiation, which is not the same as the conventional CM voltage between the ground and the circuit. A similar definition has been used in other papers [26], [28]. The CM impedance is defined as the

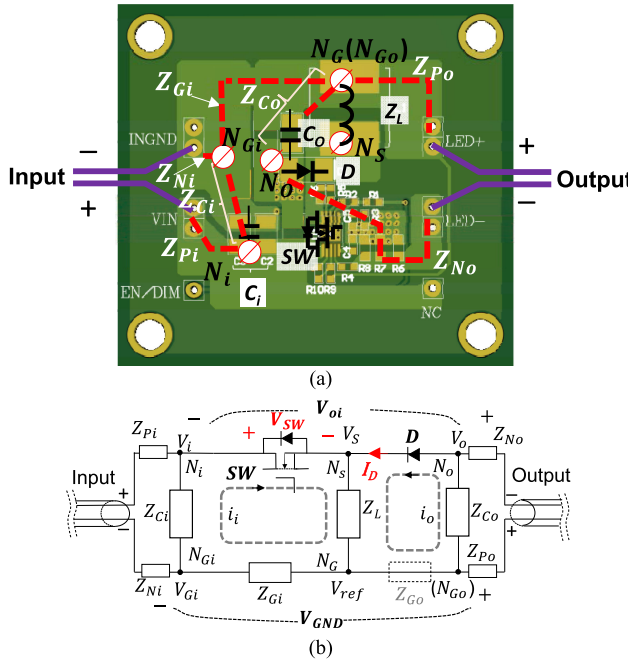


Fig. 2. Circuit model with parasitic impedances. (a) PCB layout. (b) Converter circuit model with parasitic impedances.

impedance on the CM current path in the converter model, which is not necessarily between the ground and the circuit. The cables can be modeled as an antenna impedance which is composed of a reactance X_A representing the near field energy, a resistance R_r representing the radiated energy, and a resistance R_L representing the power loss on the cables [29]. The excitation voltage added to the antenna is V_A and the CM current is I_{CM} . The excitation voltage drives the antenna and generates radiated EMI. The radiative EMI, different from conductive EMI which needs an earth ground to form a CM current loop to conduct the CM current, forms a loop via the EM waves between two cable antennas. The earth ground can, but not necessary, be part of this loop. The radiated current is the CM current, but earth ground is not necessary in the model.

A. Radiated EMI Noise Model of the Power Converter

In Fig. 1, ideally, if the impedance of the PCB ground between input ground node N_{Gi} and output ground node N_{Go} is zero, and the impedances of decoupling capacitors C_i and C_o are zero, the CM voltage source V_{CM} and the impedance Z_{CM} between the input and output cables are zero. Therefore, there will be no radiation from the cable antenna driven by V_{CM} . In practice, both PCB ground traces and the decoupling capacitors may have significant impedances, especially the parasitic impedances, at radiated EMI frequencies. Fig. 2(a) shows the PCB layout ($5\text{ cm} \times 4.6\text{ cm}$) of the buck-boost converter with the equivalent current paths and corresponding parasitic impedances illustrated. Fig. 2(b) shows a converter circuit with these parasitic impedances. Z_{Gi} is the PCB ground trace impedance between node N_{Gi} and N_G . Z_{Ci} is the impedance of C_i and the PCB trace connected to node N_{Gi} . In this PCB layout, node N_G and N_{Go}

TABLE I
EXTRACTED IMPEDANCES

Between Nodes	Inductance (Impedance) Name	Inductance Value (nH)
N_{Gi} and N_G	L_{Gi} (Z_{Gi})	13.49
N_{Gi} and N_i	L_{Ci} (Z_{Ci})	3.02
N_G and N_o	L_{Co} (Z_{Co})	2.99
INGND and N_{Gi}	L_{Ni} (Z_{Ni})	1.19
VIN and N_i	L_{Pi} (Z_{Pi})	2.41
N_{Ni} and LED+	L_{Po} (Z_{Po})	4.49
N_o and LED-	L_{Po} (Z_{Po})	10.02

merge. In a different PCB layout, if there is an impedance Z_{Go} between N_G and N_{Go} , the model should include Z_{Go} . Z_{Co} is the impedance of C_o and the PCB trace connected to node N_G . Z_L is the inductor's impedance and is approximately equal to an $8.9\text{ }\mu\text{H}$ inductance in parallel with a 45.8 pF capacitance based on impedance measurement. Z_{Pi} and Z_{Ni} are impedances between node N_i and the input cable, between node N_{Gi} and the input cable, respectively. Z_{Po} and Z_{No} are impedances between node N_G and the output cable, between node N_o and the output cable, respectively.

The impedances (inductance) of the PCB layout in Fig. 2(b) were extracted using Ansys Q3D in Table I. Because at high frequencies, both C_i and C_o branches are dominated by their equivalent series inductance (ESL), only the inductance is shown here. There are also mutual inductances between these self-inductances; however, since they are much smaller than the self-inductances, they are ignored in the analysis.

To avoid the loading effect of cable antenna on the V_{CM} and Z_{CM} extraction in Fig. 1(b) based on Fig. 2(b), the cable lengths were first minimized and ferrite beads (Fair-Rite 0431167281) were added to the input and output cables on the ends close to the PCB [15], [19]. Because the high impedance of ferrite beads effectively isolates the cable antenna, the loading effect of the cable antenna on V_{CM} and Z_{CM} in Fig. 1(b) is minimized. According to the Thevenin theorem, the equivalent Thevenin voltage is equal to the terminal voltage without the load connected [18], [23], therefore, V_{CM} is the equivalent Thevenin voltage. Z_{CM} can be extracted correspondingly based on the Thevenin theorem.

In Fig. 2(b), switching current i_i in the input loop generates voltage drops on Z_{Gi} and Z_{Ci} . Switching current i_o in the output loop generates the voltage drop on Z_{Co} . If node N_G is the voltage reference, the average voltage V_{CMi} at the input is

$$V_{CMi} = \frac{V_i + V_{Gi}}{2} \quad (1)$$

where V_i and V_{Gi} are the voltage potentials at nodes N_i and N_{Gi} . The average voltage V_{CMo} at the output is

$$V_{CMo} = \frac{V_o}{2} \quad (2)$$

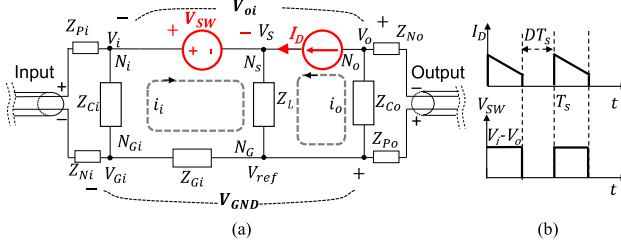


Fig. 3. Noise model. (a) Noise model with substitution theorem applied. (b) Time-domain waveforms of noise sources.

where V_o is the voltage potential at node N_o . The equivalent Thevenin CM noise voltage V_{CM} added between the input and output cables is, therefore

$$\begin{aligned} V_{CM} &= V_{CMo} - V_{CMI} = \frac{V_o - V_i}{2} + \frac{-V_{Gi}}{2} \\ &= \frac{1}{2} (V_{oi} + V_{GND}). \end{aligned} \quad (3)$$

In Fig. 2(b), if Z_{Ci} and Z_{Co} are much smaller than Z_{Gi} , the voltage drops on Z_{Ci} and Z_{Co} can be ignored, then V_{oi} is equal to V_{GND} , and V_{CM} will be equal to V_{GND} in (3). This implies that V_{GND} may predominantly determine V_{CM} , which drives the cable antenna to generate the radiated EMI.

In Fig. 2(b), based on the substitution theory, for noise analysis, the MOSFET can be substituted with a voltage source V_{SW} , which has the same voltage waveform as the MOSFET and the diode can be substituted with a current source I_D , which has the same current waveform as the diode [18], [20]–[23]. The converter noise model is therefore developed in Fig. 3.

Because Z_{Pi} , Z_{Ni} , Z_{Po} , and Z_{No} are in series with 1.5 m input and 0.5 m output cables and they are much smaller than the impedance of input and output cables, they can be ignored. The differential mode (DM) impedances of input and output cables are in parallel with and much bigger than Z_{Ci} and Z_{Co} , so they are considered open. Based on the superposition theory, the contribution of the V_{SW} or I_D to V_{CM} can be analyzed after shorting other voltage sources and disconnecting other current sources as in Fig. 4.

In Fig. 4(a), the contribution of V_{SW} to V_{oi} is $-V_{SW} \cdot (Z_{Gi} + Z_{Ci}) / (Z_{Gi} + Z_L + Z_{Ci})$, and the contribution of V_{SW} to V_{GND} is $-V_{SW} \cdot Z_{Gi} / (Z_{Gi} + Z_L + Z_{Ci})$; therefore, from (3), we obtain

$$V_{CMV} \approx -V_{SW} \cdot \frac{Z_{Gi} + Z_{Ci}/2}{Z_{Gi} + Z_L + Z_{Ci}}. \quad (4)$$

Based on (4), the transfer function G_{GV} is derived as

$$G_{GV} = \frac{V_{CMV}}{V_{SW}} \approx -\frac{Z_{Gi} + Z_{Ci}/2}{Z_{Gi} + Z_L + Z_{Ci}}. \quad (5)$$

Similarly, in Fig. 4(b), the contribution of I_D to V_{oi} is $-I_D \cdot ((Z_{Gi} + Z_{Ci}) \| Z_L + Z_{Co})$, and the contribution of I_D to V_{GND} is $-I_D \cdot ((Z_{Gi} + Z_{Ci}) \| Z_L) Z_{Gi} / (Z_{Gi} + Z_{Ci})$, so from (3), we obtain

$$\begin{aligned} V_{CMI} &\approx -0.5 I_D \cdot ((Z_{Gi} + Z_{Ci}) \| Z_L) Z_{Gi} / (Z_{Gi} + Z_{Ci}) \\ &+ ((Z_{Gi} + Z_{Ci}) \| Z_L + Z_{Co}). \end{aligned} \quad (6)$$

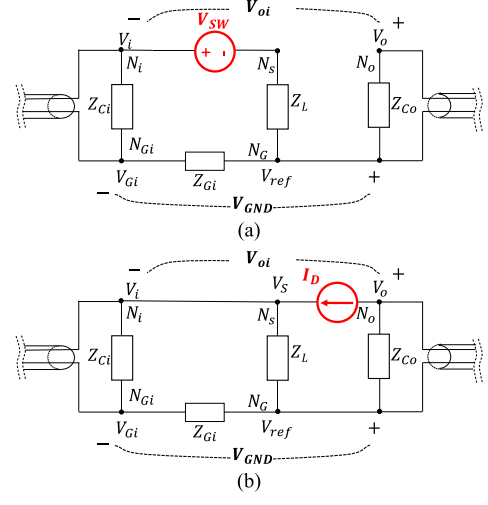


Fig. 4. Contributions of (a) V_{SW} and (b) I_D to V_{CM} .

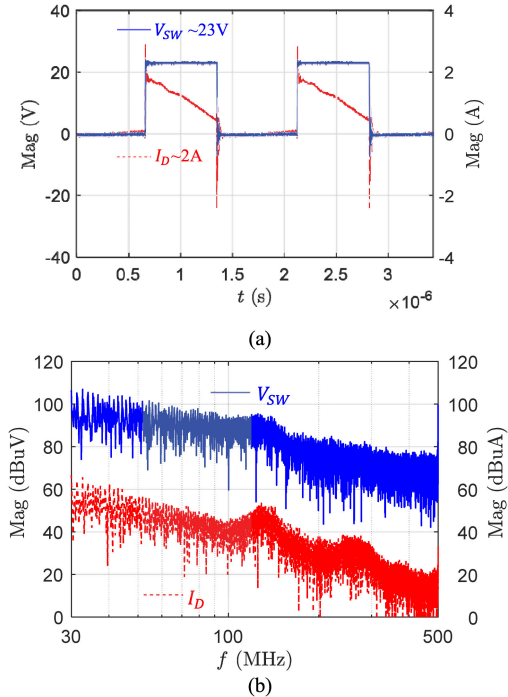


Fig. 5. Noise voltage and current sources. (a) Waveforms. (b) Spectra.

The transfer function G_{GI} is derived as

$$\begin{aligned} G_{GI} &= \frac{V_{CMI}}{I_D} \approx -0.5[((Z_{Gi} + Z_{Ci}) \| Z_L) Z_{Gi} / (Z_{Gi} + Z_{Ci}) \\ &+ ((Z_{Gi} + Z_{Ci}) \| Z_L + Z_{Co})]. \end{aligned} \quad (7)$$

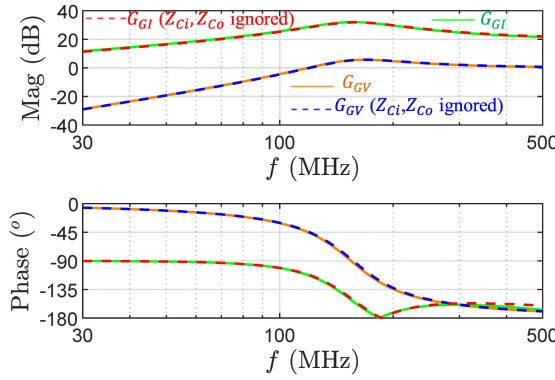
According to the superposition theorem, we have

$$V_{CM} \approx V_{CMV} + V_{CMI} \quad (8)$$

or

$$V_{CM} \approx V_{SW} \cdot G_{GV} + I_D \cdot G_{GI}. \quad (9)$$

The measured switching waveforms of V_{SW} and I_D are shown in Fig. 5(a). It should be noted that a current sensing

Fig. 6. Noise transfer gains of G_{GV} and G_{GI} .

resistor (0805 0.1 Ω) is connected in series with the diode for I_D measurement. To extract frequency, phase, and magnitude information with fast Fourier transform (FFT), the sampling rate of the oscilloscope in the measurement should be at least twice of the highest concerned frequency [30]. For example, when the highest concerned frequency is 500 MHz, the sampling rate should be more than 1 GSa/s. Furthermore, in order not to lose the information of each harmonic component, the time-domain signal used for FFT calculation should have at least one or more number of whole period waveform [30].

The spectra of V_{SW} and I_D are shown in Fig. 5(b). In this application, V_{SW} is much higher than I_D . Because the upper band of the voltage probes (Rigol RP3500A) used for V_{SW} and I_D measurements is 500 MHz, the EMI above 500 MHz is not discussed in the article.

The noise transfer gains G_{GV} and G_{GI} are calculated in Fig. 6 based on (5), (7), and the extracted impedances in Table I.

In Table I, since Z_{Ci} and Z_{Co} are much smaller than Z_{Gi} and Z_L , (5) and (7) can be simplified to

$$G_{GV} = \frac{V_{CMV}}{V_{SW}} \approx -\frac{Z_{Gi}}{Z_{Gi} + Z_L} \quad (10)$$

$$G_{GI} = \frac{V_{CMI}}{I_D} \approx -Z_{Gi}||Z_L. \quad (11)$$

Fig. 6 shows the comparison of G_{GV} and G_{GI} before and after the simplification. The simplification does not introduce any observable errors, so Z_{Ci} and Z_{Co} will be ignored in this article. As a result, $V_{oi} \approx V_{GND}$ and based on (3), V_{CM} will be

$$V_{CM} \approx V_{GND}. \quad (12)$$

The impedance of PCB ground therefore plays a critical role in the radiated EMI. Based on the converter noise models in Fig. 4, the Thevenin equivalent impedance Z_{CM} in Fig. 1(b) is

$$Z_{CM} \approx (Z_{Gi}||Z_L). \quad (13)$$

The impedance curve of Z_{CM} is shown in Fig. 7.

The predicted V_{CM} spectrum based on (9), Figs. 5 and 6 is shown in Fig. 8. V_{CM} spectrum is also measured using a wideband oscilloscope with 1 $M\Omega$ input impedance. Because the input impedance is much higher than Z_{CM} in Fig. 7, the voltage probe does not have loading effects on V_{CM} so the measured V_{CM} is accurate. The measured is compared with the

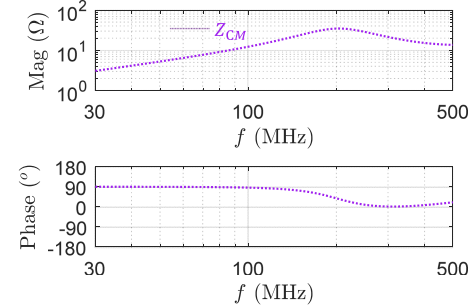
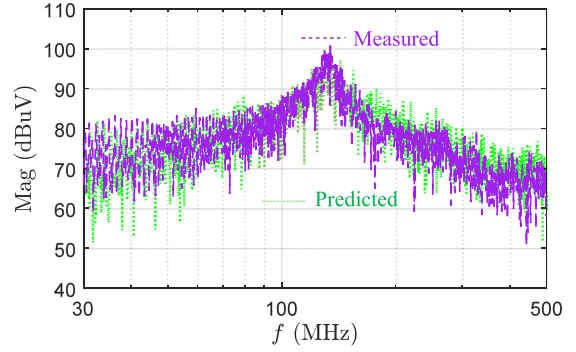
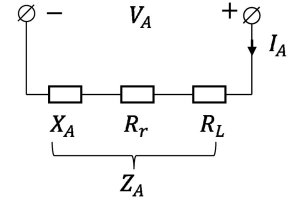
Fig. 7. Thevenin CM impedance Z_{CM} .Fig. 8. Comparison of the measured and predicted spectra of V_{CM} .

Fig. 9. Equivalent antenna impedance model.

predicted in Fig. 8. They match very well, which verifies the developed noise model.

The calculation also found that for this case, although G_{GI} is bigger than G_{GV} , because V_{SW} is much higher than I_D , the contribution of V_{SW} to V_{CM} is dominant above 30 MHz.

In summary, both the switching current source I_D and voltage source V_{SW} generate switching currents in the input loop $SW-Z_L-Z_{Gi}-Z_{Ci}$. The currents further generate voltage drop on the ground impedance Z_{Gi} on the converter's PCB (the ground is the negative bus of the converter, not the earth ground). The voltage drop V_{CM} on Z_{Gi} in turn works as the driving voltage for the cable antenna to generate CM noise and the radiated EMI. This mechanism indicates that DM currents and voltages can be transformed to the excitation voltages on Z_{Gi} and further lead to radiated EMI.

B. Cable Antenna Model

The circuit model of the cable antenna has been discussed in Fig. 1(b) and is shown in Fig. 9 with the excitation voltage V_A . The cable antenna model represents not only the cables but also the LED loads, the voltage source, and other items such as

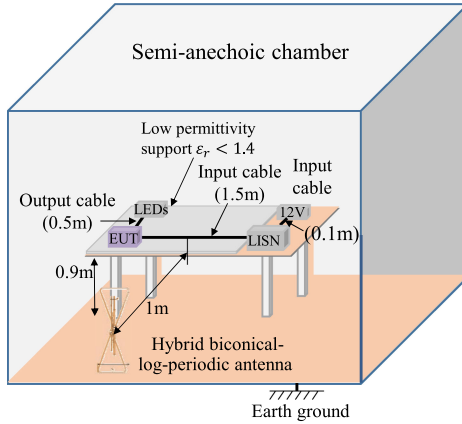


Fig. 10. Radiated EMI measurement setup in a semianechoic chamber.

LISNs connected to the cables, as specified in standard CISPR 25 in Fig. 10.

The radiated power P_r on R_r can be predicted based on the model in Fig. 9. The antenna transfer function G_{VA} from $|V_A|$ to the maximum radiated electric field intensity E_{\max} at distance r from the converter is $G_{VA} = \frac{E_{\max}}{|V_A|}$ [18].

G_{VA} can be experimentally extracted in a semianechoic chamber based on the radiated EMI measurement setup in Fig. 10 with the equipment under test (EUT) (converter) replaced with an RF signal generator. In the experiments, a 0.5 m output cable was used to connect the converter's output to the LED load. A 1.5 m input cable is perpendicular to the output cable and connects the input of the converter to two LISNs. A 0.1 m cable further connects the LISNs to a 12-V battery. All of these cables are composed of two twisted AWG16 wires. The EUT (converter) was removed from the cables with cables untouched. The terminals of the two conductors of the cables were shorted on the converter sides. The excitation voltage V_A generated from an RF generator (Rigol DSG830) is added to the cable terminals where the converter was originally connected via a wideband unbalance-to-balance transformer (Mini-Circuit FTB-1-1*A15+). High-frequency ferrite beads (Fair-Rite 0431167281) are added to the RF signal generator's output cable and the transformer's output cable to minimize their couplings to the cable antenna [19]. E_{\max} was measured using a receiving antenna (SUNAR RF MOTION JB3) at a distance 1 m away as in Fig. 10.

The extracted G_{VA} is shown in Fig. 11. It has bumps around 83, 130, 200, 250, 300, and 400 MHz and these bumps may lead to EMI spikes in the spectrum of the finally measured radiated EMI.

The cable antenna impedance Z_A is measured based on a technique proposed in [23] with a vector network analyzer (VNA) (Copper Mountain Planar808/1). The ferrite beads (Fair-Rite 0431167281) were implemented on the coaxial cables of the VNA to reduce the couplings between the coaxial cables and the converter's input and output cables, as shown in Fig. 12(a). This can improve the measurement accuracy [23]. In Fig. 12(b), the measured Z_A is compared with Z_{CM} , which was derived from (13) and shown in Fig. 7. Z_A is much higher than Z_{CM} . As

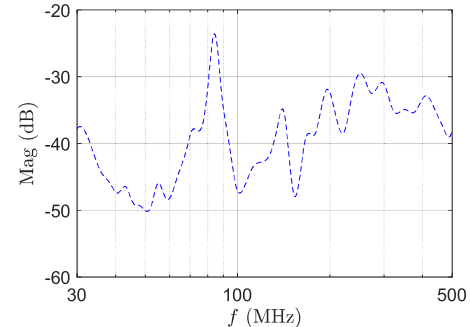


Fig. 11. Extracted antenna transfer gain G_{VA} .

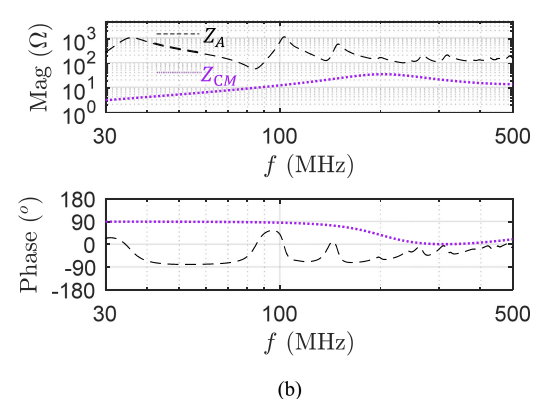
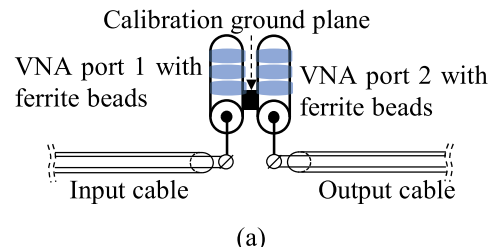


Fig. 12. Extraction of cable antenna impedance. (a) Measurement setup diagram [23]. (b) Comparison of the source impedance Z_{CM} and the cable antenna impedance Z_A .

a result, based on Fig. 1(b), the radiation excitation voltage V_A will be mostly equal to V_{CM} (or V_{GND}), which is the voltage drop on Z_{Gi} . Since the impedance of PCB ground plays a big role in Z_{CM} as shown in (13), it is very critical to the radiated EMI.

C. Radiated EMI Prediction and Analysis

The radiated EMI can be predicted based on Figs. 8 and 11. The predicted is compared with the measured average EMI in Fig. 13. The radiated EMI measurement was conducted based on the setup in Fig. 10. Based on CISPR 25, the resolution bandwidth (RBW) of the spectrum analyzer is set to 120 kHz for the radiated EMI measurement. Based on [30], because RBW is much smaller than the switching frequency 700 kHz, there is only one harmonic within 2RBW. As a result, the measured peak, quasi-peak, and average EMI are equal. Because of this, the predicted EMI spectrum based on FFT in Fig. 8 will be equal to the predicted average EMI. The comparison in Fig. 13 is therefore

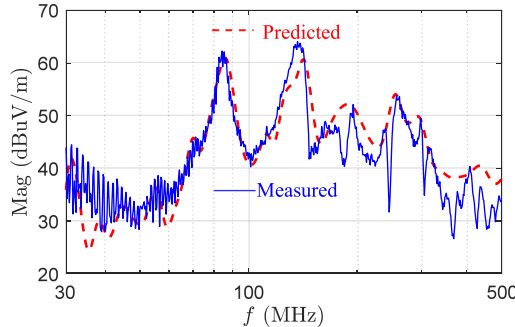


Fig. 13. Comparison of the measured and predicted radiated EMI.

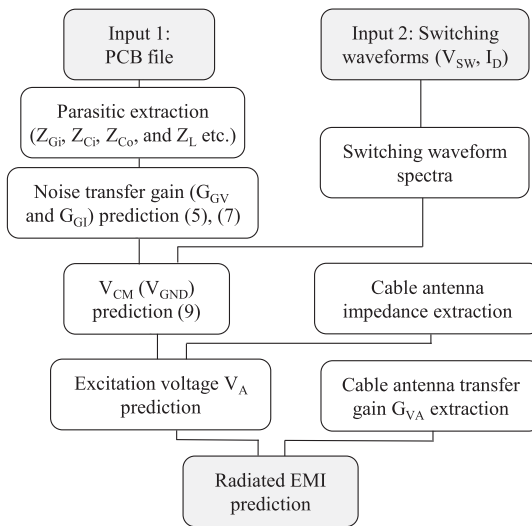


Fig. 14. Flowchart for radiated EMI prediction.

the predicted average EMI versus the measured average EMI. It is shown that the predicted approximately matches the measured from 30 to 500 MHz. It should be noted that the discrepancy between the prediction and measurement around 40, 190, and 380 MHz could be caused by two factors: 1) the discrepancy in V_{CM} extraction due to the inaccuracy of waveform measurement and parasitic impedance extraction; 2) the discrepancy in G_{VA} extraction due to the limited resolution of the spectrum analyzer at the frequencies where the cable antenna has low G_{VA} and low E_{max} .

The major EMI spikes at 83, 130, 200, 250, and 400 MHz in Fig. 13 are due to the bumps of the cable antenna's transfer gain G_{VA} in Fig. 11. The G_{VA} 's small bump around 130 MHz was amplified by the spike of V_{CM} 's spectrum around 130 MHz in Fig. 8; as a result, the EMI spike around 130 MHz is the highest. This indicates that both V_{CM} and G_{VA} are critical to the radiated EMI. Since G_{VA} is determined by the measurement setup and the product's cable specifications, the radiated EMI should be suppressed by reducing V_{CM} , i.e., V_{GND} .

In general, the radiated EMI model of a non-isolated power converter can be developed and the radiated EMI can be predicted based on the flowchart in Fig. 14. The PCB ground impedance can be extracted based on the PCB layout using software such as Ansys Q3D. The spectra of switching voltage and

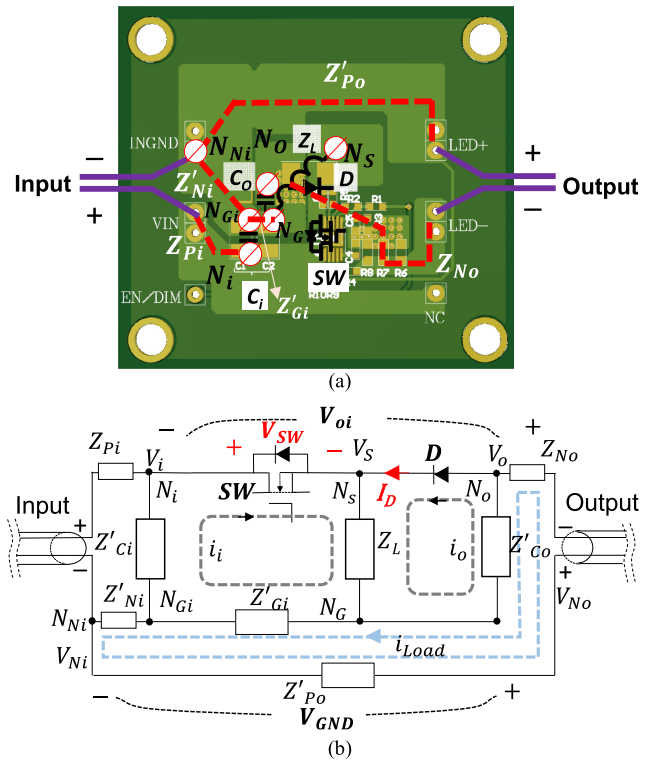


Fig. 15. Improved power converter layout. (a) Improved PCB layout. (b) Converter circuit with parasitics.

current waveforms can be extracted with FFT from the measured time-domain waveforms using a wideband oscilloscope.

III. TECHNIQUES OF RADIATED EMI REDUCTION

A. Improving Power Converter Layout

Based on the analysis in Section II, the excitation voltage V_A of the cable antenna is due to the voltage drop of switching currents on PCB ground impedance Z_{Gi} between the input and output cables. Therefore, V_A can be reduced by reducing Z_{Gi} with an optimal PCB layout. V_A can also be reduced by keeping switching current out of the ground impedance such as Z'_{Ni} , Z'_{Po} , and Z_{No} between the input and output cables. Fig. 15 shows an improved PCB layout and circuit model with parasitics based on this technique.

Compared with the PCB layout in Fig. 2, the layout of inductor L and output capacitor C_o has been optimized in Fig. 15(a). Their grounding terminals have been moved to very close to the grounding terminal of C_i , as in Fig. 15(a). These grounding terminals are not on the path of the ground impedance Z'_{Po} between the input and output cables. The converter circuit parasitic model is developed in Fig. 15(b). The parasitic impedances were extracted using Ansys Q3D in Table II. Z_{Gi} has been significantly reduced to Z'_{Gi} (1.95 nH) from 13.49 nH (17 dB reduction).

From Fig. 15(b), the switching currents i_i and i_o do not flow through Z'_{Ni} , Z'_{Po} , and Z_{No} . The currents flowing through these impedances are mostly dc. As a result, for high-frequency EMI noise, $V_{Gi} \approx V_{Ni} \approx V_{No}$, so $V_{GND} = V_{No} - V_{Ni} \approx 0$. The average

TABLE II
EXTRACTED IMPEDANCES OF THE IMPROVED LAYOUT

Between nodes	Inductance (impedance) Name	Inductance Value (nH)
N_{Gi} and N_G	L'_{Gi} (Z'_{Gi})	1.95
N_{Gi} and N_i	L'_{Ci} (Z'_{Ci})	1.05
N_G and N_o	L'_{Co} (Z'_{Co})	0.98
INGND and N_{Gi}	L'_{Ni} (Z'_{Ni})	2.61
N_{Ni} and LED+	L'_{Po} (Z'_{Po})	15.21

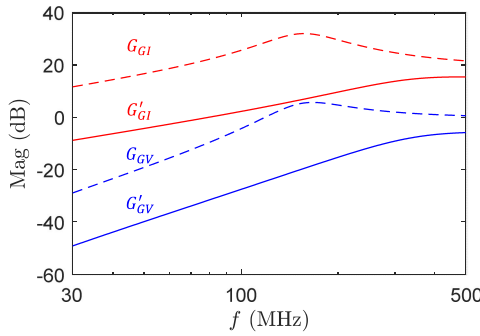


Fig. 16. Voltage and current transfer function comparison.

voltage V_{CMi} at the input is

$$V_{CMi} = \frac{V_i + V_{Gi}}{2}. \quad (14)$$

The average voltage V_{CMo} at the output is

$$V_{CMo} = \frac{V_{Ni} + V_o}{2}. \quad (15)$$

The equivalent Thevenin CM noise voltage source V_{CM} added between the input and output cables is therefore

$$V_{CM} = V_{CMo} - V_{CMi} \approx \frac{V_o - V_i}{2} = \frac{1}{2} V_{oi}. \quad (16)$$

Based on substitution and superposition theories, since $Z_L \gg Z'_{Ci}, Z'_{Co}$, V_{CM} can be calculated as

$$\begin{aligned} V_{CM} &= G'_{GV} V_{SW} + G'_{GI} I_D \\ &\approx -\frac{1}{2} \left[\frac{Z'_{Ci} + Z'_{Gi}}{Z'_{Ci} + Z'_{Gi} + Z_L} \right] V_{SW} \\ &\quad - \frac{1}{2} [(Z'_{Ci} + Z'_{Gi}) // Z_L + Z'_{Co}] I_D. \end{aligned} \quad (17)$$

Both G'_{GV} and G'_{GI} are much smaller than G_{GV} in (5) and G_{GI} in (7) of the original PCB layout, as shown in Fig. 16. Similar to the original PCB layout, Z_{CM} is much smaller than cable antenna impedance Z_A , so $V_A = V_{CM}$.

Because of the significantly reduced G_{GV} and G_{GI} , Fig. 17(a) shows that the measured V_{CM} is significantly reduced in the whole frequency range. As a result, the measured radiated EMI is significantly reduced as shown in Fig. 17(b), which verifies the proposed technique.

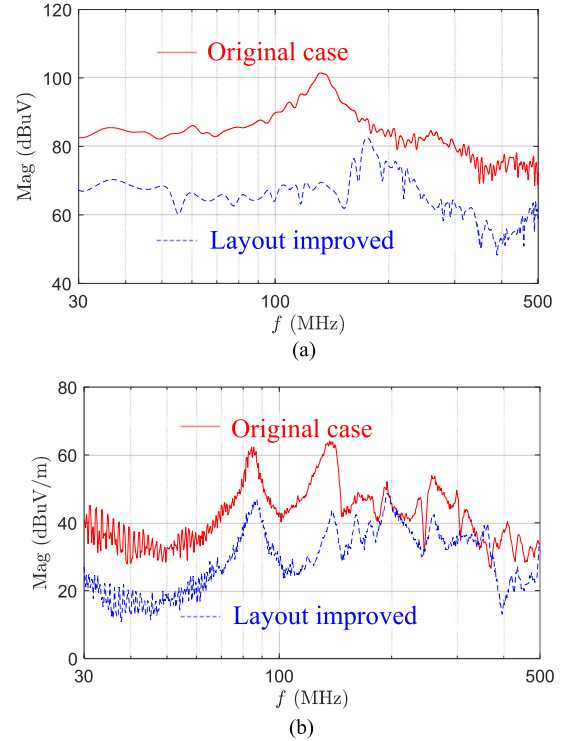


Fig. 17. Radiated EMI before and after the layout improvement. (a) Comparison of V_{CM} . (b) Comparison of the measured radiated EMI.

In summary, with the given radiated EMI measurement setup and the antenna transfer gain, improving the power converter's PCB layout can greatly reduce V_{CM} , and therefore, greatly reduce the radiated EMI in the whole frequency range. Specifically, to reduce V_{CM} , the grounding terminals of C_i , L , and C_o should be as close as possible to reduce Z_{Gi} and Z_{Go} , if any, because their currents are discontinuous switching currents.

B. Radiated EMI Reduction With a Cross Capacitor

In the original PCB layout, because nodes N_i and N_o are very close; the power converter's ground parasitic impedance can be equivalently reduced by adding a capacitor C_r with a small impedance between N_i and N_o to reduce V_A without changing the original PCB layout as in Fig. 18.

The small impedance of C_r can help greatly reduce V_{GND} because it is efficiently in parallel with Z_{Gi} . C_r is added between nodes N_i and N_o instead of between N_{Gi} and N_G because the N_i and N_o have a much shorter distance than N_{Gi} and N_G so C_r can have better high-frequency performance with much smaller ESL. With C_r applied, the G_{GV} and G_{GI} in (10) and (11) become

$$G_{GV} = \frac{V_{CMV}}{V_{SW}} \approx -\frac{Z_{Gi} // Z_{Cr}}{Z_{Gi} // Z_{Cr} + Z_L} \quad (18)$$

$$G_{GI} = \frac{V_{CMI}}{I_D} \approx -Z_{Gi} // Z_{Cr} // Z_L. \quad (19)$$

In the experiment, a 1 μ F ceramic capacitor (SMD 1210, ESL 0.98 nH) is used as C_r . Its high-frequency impedance is determined by its ESL, much smaller than $L_{Gi} = 13.49$ nH. The

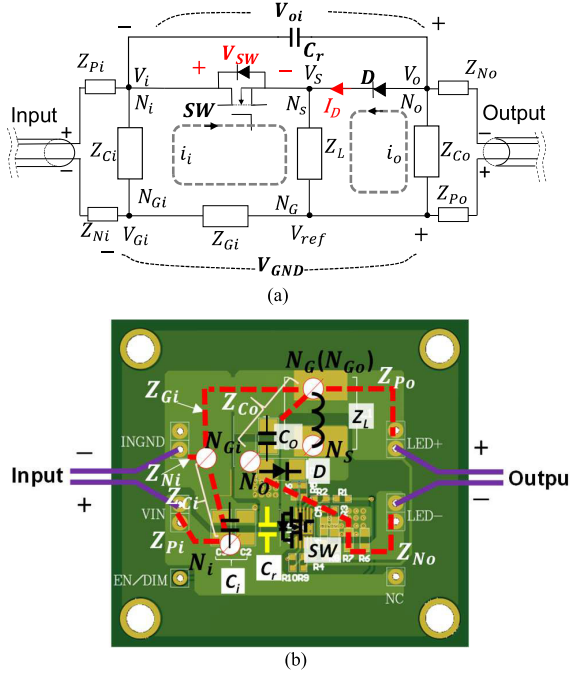


Fig. 18. Cross capacitor to reduce radiated EMI. (a) Circuit. (b) PCB layout.

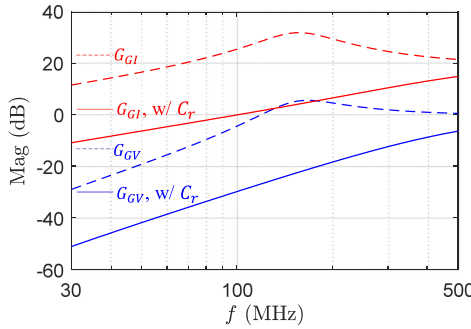


Fig. 19. Comparison of G_{GV} and G_{GI} before and after adding C_r .

G_{GV} and G_{GI} are greatly reduced compared with the original layout without C_r , as shown in Fig. 19.

C_r only has a slight influence on switching transients. Fig. 20(a) and (b) shows the time-domain waveforms of V_{SW} as well as the spectrum of V_{SW} . The ringing amplitude on the rising and falling edges is slightly increased but they are well below the safety voltage. Compared with the original layout, at frequencies <120 MHz, the spectrum is almost unchanged. From 120 to 300 MHz, the spectrum is slightly increased. However, since G_{GV} and G_{GI} are significantly reduced, the spectrum of $V_{GND}(V_{CM})$ is significantly reduced compared with the original layout without C_r in Fig. 21.

Because V_{CM} is significantly reduced, the measured radiated EMI is greatly reduced with C_r added, as shown in Fig. 22. It has been verified that with the same radiated EMI measurement setup and the antenna transfer gain as in the improved PCB layout case in Section III-A, adding C_r can also greatly reduce V_{CM} , and therefore, greatly reduce radiated EMI.

For these two radiated EMI reduction techniques, PCB layout improvement is cost-free, therefore a better approach if it is

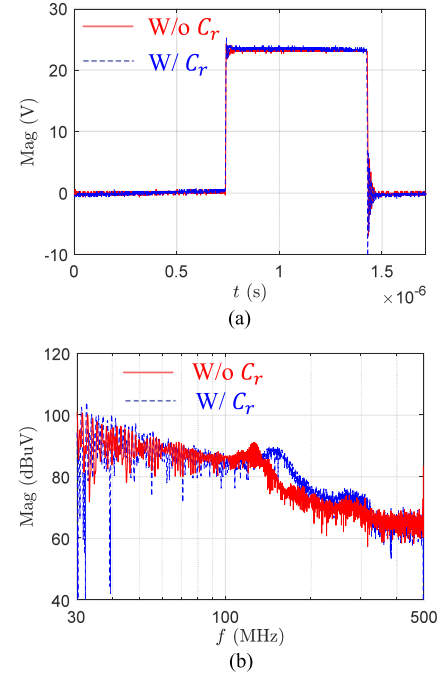


Fig. 20. V_{SW} before and after C_r is added. (a) Waveform. (b) Spectra.

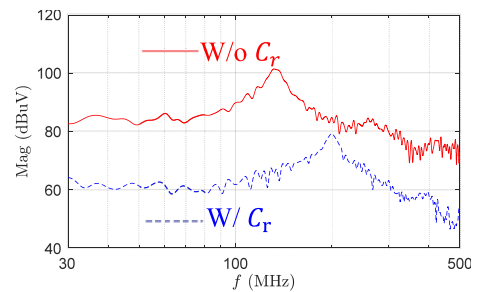


Fig. 21. Spectra of $V_{GND}(V_{CM})$ before and after C_r is added.

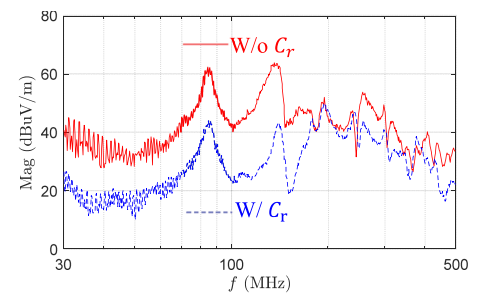


Fig. 22. Measured radiated EMI before and after a cross capacitor is added.

implemented at an early stage of the power converter design. Adding a cross capacitor C_r is an alternative at the end of the power converter design stage when the PCB layout modification is not preferred.

In summary, with the identical radiated EMI measurement setup and the antenna transfer gain, both techniques can significantly reduce the radiated EMI in the whole frequency range. If Z_{Gi} or Z_{Go} cannot be minimized but nodes N_i and

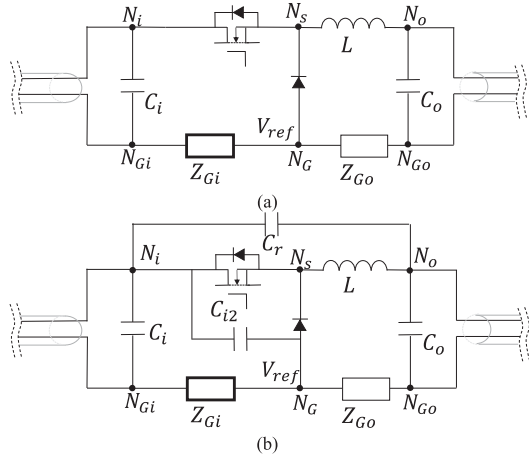


Fig. 23. Analysis of a buck converter. (a) Critical ground impedance in a buck converter. (b) Techniques to reduce radiated EMI.

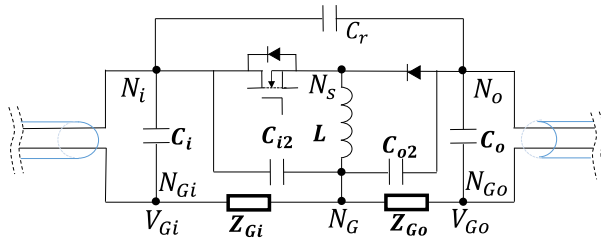


Fig. 24. C_{i2} and C_{o2} can reduce V_{CM} and radiated EMI in a buck-boost converter.

N_o are very close, a cross capacitor can be used to equivalently reduce the ground impedance and V_{CM} .

IV. APPLYING TO OTHER NON-ISOLATED POWER CONVERTER TOPOLOGIES WHEN THE DOMINANT ELECTRIC FIELD IS DUE TO THE VOLTAGE DROP ON THE GROUND IMPEDANCE

The proposed modeling, analysis, and reduction techniques for radiated EMI in an automotive non-isolated converter can be extended to other power converter topologies such as buck and boost converters when the dominant electric field is due to the voltage drop on the ground impedance.

Fig. 23(a) shows a buck converter. Z_{Gi} is identified as the critical ground impedance for radiated EMI because of the discontinuous switching current flowing through it. On the other hand, Z_{Go} is not critical as its current is continuous inductor current, unless the converter operates in discontinuous conduction mode. To reduce Z_{Gi} , the grounding terminals of C_i and the diode should be as close as possible. A cross capacitor can be added between nodes N_i and N_o to reduce V_{CM} if nodes N_i and N_o are very close, as shown in Fig. 23(b). In Fig. 23, C_{i2} is also used to equivalently reduce Z_{Gi} and V_{CM} if nodes N_i and N_G are very close. The same technique can also be applied to buck-boost converters. C_{i2} and C_{o2} are added between nodes N_i , N_o , and N_G to equivalently reduce critical impedances Z_{Gi} and Z_{Go} , and therefore V_{CM} in Fig. 24 if they are very close.

Fig. 25(a) shows a boost converter. Z_{Go} is identified as the critical ground impedance for radiated EMI because of the discontinuous switching current flowing through it. On the other

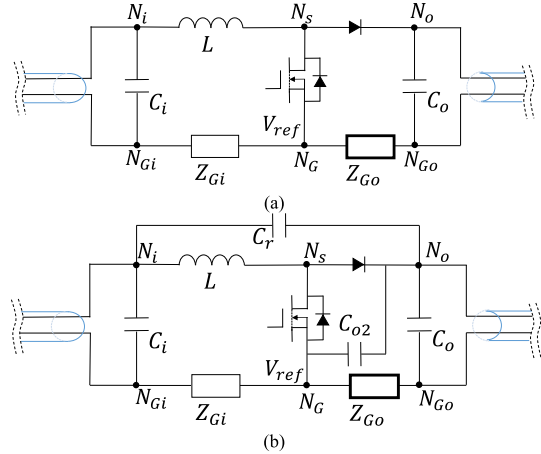


Fig. 25. Analysis of a boost converter. (a) Critical ground impedance in a boost converter. (b) Techniques to reduce radiated EMI.

hand, Z_{Gi} is not critical as its current is continuous inductor current, unless the converter operates in discontinuous conduction mode. To reduce Z_{Go} , the grounding terminals of C_o and the main switch should be as close as possible. A cross capacitor can be added between nodes N_i and N_o to reduce V_{CM} if nodes N_i and N_o are very close, as shown in Fig. 25(b). In Fig. 25(b), C_{o2} is also used to equivalently reduce Z_{Go} and V_{CM} if nodes N_o and N_G are very close.

V. CONCLUSION

This article developed and quantified a radiated EMI noise model for non-isolated power converters based on PCB parasitics and converter operation principles. Based on the analysis of the developed model, it has been identified that the voltage drop of the switching currents on the PCB ground impedance between the input and output cables plays an important role in the radiated EMI. It is also found the radiated EMI spikes are caused by both cable antenna and equivalent noise voltage source. A technique to develop radiated EMI models for non-isolated power converters was proposed. Two techniques were proposed to greatly reduce radiated EMI. One is PCB layout optimization to reduce PCB ground impedance and keep switching currents out of the direct impedance path between the input and output cables. The other one is adding a cross capacitor between the input and output to equivalently reduce the PCB ground impedance. Experiments were conducted to validate the developed techniques. The proposed techniques are also extended to other converter topologies when the dominant electric field is due to the voltage drop on the ground impedance.

REFERENCES

- [1] C. Nan, R. Ayyanar, and Y. Xi, "A 2.2-MHz active-clamp buck converter for automotive applications," *IEEE Trans. Power Electron.*, vol. 33, no. 1, pp. 460–472, Jan. 2018.
- [2] V. Rodriguez, "Automotive component EMC testing: CISPR 25, ISO 11452-2 and equivalent standards," *IEEE Electromagn. Compat. Mag.*, vol. 1, no. 1, pp. 83–90, Jan. 2012.
- [3] C. F. M. Carobbi and D. Izzo, "Evaluation and improvement of the reproducibility of CISPR 25 ALSE test method," *IEEE Trans. Electromagn. Compat.*, vol. 60, no. 4, pp. 1069–1077, Aug. 2018.

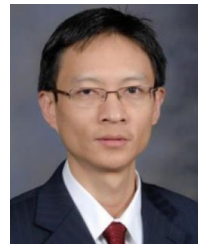
- [4] B. Zhang and S. Wang, "A survey of EMI research in power electronics systems with wide bandgap semiconductor devices," *IEEE J. Emerg. Sel. Topics Power Electron.*, vol. 8, no. 1, pp. 626–643, Mar. 2020.
- [5] J. Zhang, T. Lu, W. Zhang, X. Bian, and X. Cui, "Characteristics and influence factors of radiated disturbance induced by IGBT switching," *IEEE Trans. Power Electron.*, vol. 34, no. 12, pp. 11833–11842, Dec. 2019.
- [6] L. Middelstaedt, J. Wang, B. H. Stark, and A. Lindemann, "Direct approach of simultaneously eliminating EMI-critical oscillations and decreasing switching losses for wide bandgap power semiconductors," *IEEE Trans. Power Electron.*, vol. 34, no. 11, pp. 10376–10380, Nov. 2019.
- [7] J. Jia, D. Rinas, and S. Frei, "Predicting the radiated emissions of automotive systems according to CISPR 25 using current scan methods," *IEEE Trans. Electromagn. Compat.*, vol. 58, no. 2, pp. 409–418, Apr. 2016.
- [8] S. Hwan-Woo and T. H. Hubing, "Model for estimating radiated emissions from a printed circuit board with attached cables due to voltage-driven sources," *IEEE Trans. Electromagn. Compat.*, vol. 47, no. 4, pp. 899–907, Nov. 2005.
- [9] D. M. Hockanson, J. L. Drewniak, T. H. Hubing, T. P. V. Doren, S. Fei, and M. J. Wilhelm, "Investigation of fundamental EMI source mechanisms driving common-mode radiation from printed circuit boards with attached cables," *IEEE Trans. Electromagn. Compat.*, vol. 38, no. 4, pp. 557–566, Nov. 1996.
- [10] F. Costa, C. Gautier, B. Revol, J. Genoulaz, and B. Démoulin, "Modeling of the near-field electromagnetic radiation of power cables in automotives or aeronautics," *IEEE Trans. Power Electron.*, vol. 28, no. 10, pp. 4580–4593, Oct. 2013.
- [11] G. Ala, M. C. D. Piazza, G. Tine, F. Viola, and G. Vitale, "Evaluation of radiated EMI in 42-V vehicle electrical systems by FDTD simulation," *IEEE Trans. Veh. Technol.*, vol. 56, no. 4, pp. 1477–1484, Jul. 2007.
- [12] G. Ala, M. C. D. Piazza, G. Tine, F. Viola, and G. Vitale, "Numerical simulation of radiated EMI in 42 V electrical automotive architectures," *IEEE Trans. Magn.*, vol. 42, no. 4, pp. 879–882, Apr. 2006.
- [13] M. Laour, R. Tahmi, and C. Vollaire, "Modeling and analysis of conducted and radiated emissions due to common mode current of a buck converter," *IEEE Trans. Electromagn. Compat.*, vol. 59, no. 4, pp. 1260–1267, Aug. 2017.
- [14] A. Radchenko *et al.*, "Transfer function method for predicting the emissions in a CISPR-25 test-setup," *IEEE Trans. Electromagn. Compat.*, vol. 56, no. 4, pp. 894–902, Aug. 2014.
- [15] S. Shinde *et al.*, "Radiated EMI estimation from DC-DC converters with attached cables based on terminal equivalent circuit modeling," *IEEE Trans. Electromagn. Compat.*, vol. 60, no. 6, pp. 1769–1776, Dec. 2018.
- [16] C. Zietz, G. Armbrecht, T. Schmid, M. Wollitzer, and B. Geck, "A general calibration procedure for measuring RF voltages and currents applied to the EMC analysis of automotive high-voltage power networks," *IEEE Trans. Electromagn. Compat.*, vol. 57, no. 5, pp. 915–925, Oct. 2015.
- [17] H. Chen, T. Wang, L. Feng, and G. Chen, "Determining far-field EMI from near-field coupling of a power converter," *IEEE Trans. Power Electron.*, vol. 29, no. 10, pp. 5257–5264, Oct. 2014.
- [18] Y. Zhang, S. Wang, and Y. Chu, "Investigation of radiated electromagnetic interference for an isolated high-frequency DC–DC power converter with power cables," *IEEE Trans. Power Electron.*, vol. 34, no. 10, pp. 9632–9643, Oct. 2019.
- [19] J. He, Z. Guo, and X. Li, "Mechanism model and prediction method of common mode radiation for a non-isolated very-high-frequency DC–DC converter with cables," *IEEE Trans. Power Electron.*, vol. 35, no. 10, pp. 10227–10237, Oct. 2020.
- [20] J. Yao, Y. Li, S. Wang, X. Huang, and X. Lyu, "Modeling and reduction of radiated EMI in a GaN IC-based active clamp flyback adapter," *IEEE Trans. Power Electron.*, vol. 36, no. 5, pp. 5440–5449, May 2021.
- [21] J. Yao *et al.*, "Modeling and reduction of radiated common mode current in flyback converters," in *Proc. IEEE Energy Convers. Congr. Expo.*, 2018, pp. 6613–6620.
- [22] Y. Li, H. Zhang, S. Wang, H. Sheng, C. P. Chng, and S. Lakshminathan, "Investigating switching transformers for common mode EMI reduction to remove common mode EMI filters and Y-capacitors in flyback converters," *IEEE J. Emerg. Sel. Topics Power Electron.*, vol. 6, no. 4, pp. 2287–2301, Dec. 2018.
- [23] J. Yao, S. Wang, and H. Zhao, "Measurement techniques of common mode currents, voltages, and impedances in a flyback converter for radiated EMI diagnosis," *IEEE Trans. Electromagn. Compat.*, vol. 61, no. 6, pp. 1997–2005, Dec. 2019.
- [24] J. Yao, Y. Li, H. Zhao, and S. Wang, "Design of CM inductor based on core loss for radiated EMI reduction in power converters," in *Proc. IEEE Appl. Power Electron. Conf. Expo.*, 2019, pp. 2673–2680.
- [25] S. Wang, P. Kong, and F. C. Lee, "Common mode noise reduction for boost converters using general balance technique," *IEEE Trans. Power Electron.*, vol. 22, no. 4, pp. 1410–1416, Jul. 2007.
- [26] L. Yang, H. Zhao, S. Wang, and Y. Zhi, "Common-mode EMI noise analysis and reduction for AC–DC–AC systems with paralleled power modules," *IEEE Trans. Power Electron.*, vol. 35, no. 7, pp. 6989–7000, Jul. 2020.
- [27] S. Wang, Y. Y. Maillet, F. Wang, R. Lai, F. Luo, and D. Boroyevich, "Parasitic effects of grounding paths on common-mode EMI filter's performance in power electronics systems," *IEEE Trans. Ind. Electron.*, vol. 57, no. 9, pp. 3050–3059, Sep. 2010.
- [28] S. Wang, Y. Y. Maillet, F. Wang, D. Boroyevich, and R. Burgos, "Investigation of hybrid EMI filters for common-mode EMI suppression in a motor drive system," *IEEE Trans. Power Electron.*, vol. 25, no. 4, pp. 1034–1045, Apr. 2010.
- [29] C. Balanis, *Antenna Theory: Analysis and Design*. New York, NY, USA: Wiley Blackwell, 2016.
- [30] L. Yang, S. Wang, H. Zhao, and Y. Zhi, "Prediction and analysis of EMI spectrum based on the operating principle of EMC spectrum analyzers," *IEEE Trans. Power Electron.*, vol. 35, no. 1, pp. 263–275, Jan. 2020.



Juntao Yao (Member, IEEE) received the B.S. and M.S. degrees from Wuhan University, Wuhan, China, in 2013 and 2016, respectively, and the Ph.D. degree from the University of Florida, Gainesville, FL, USA, in 2021, all in electrical engineering.

In 2021, he joined the Apple as an EMC Design Engineer. He has authored and coauthored more than 20 IEEE journal and conference papers and holds 10 U.S./international patents. His research interests include power electronics and electromagnetic interference/electromagnetic compatibility.

Dr. Yao was the recipient of the Best Presentation Award in the Applied Power Electronics Conference in 2021.



Shuo Wang (Fellow, IEEE) received the Ph.D. degree in electrical engineering from Virginia Tech, Blacksburg, VA, USA, in 2005.

He is currently a Full Professor with the Department of Electrical and Computer Engineering, University of Florida, Gainesville, FL, USA. He has authored or coauthored more than 200 IEEE journal and conference papers and holds around 30 pending/issued U.S./international patents.

Dr. Wang was the recipient of the Best Transaction Paper Award from the IEEE Power Electronics Society in 2006 and two William M. Portnoy Awards for the papers published in the IEEE Industry Applications Society in 2004 and 2012, respectively. In 2012, he was also the recipient of the prestigious National Science Foundation CAREER Award. He is an Associate Editor for the IEEE TRANSACTIONS ON INDUSTRY APPLICATIONS and the IEEE TRANSACTIONS ON ELECTROMAGNETIC COMPATIBILITY. He is the Chair of Power Electronics EMC/EMC Special Committee of IEEE EMC Society and an Instructor of IEEE Clayton Paul Global University. He was a Technical Program Co-Chair of the IEEE 2014 International Electric Vehicle Conference.



Zheng Luo received the M.S. degree in electrical engineering from Virginia Tech, Blacksburg, VA, USA, in 2008.

He is currently a Senior Manager with Monolithic Power Systems, Inc., San Jose, CA, USA. He holds more than 20 U.S./international patents. His research interests include power electronic circuits, control, and power management ICs.